

Opposing trends of cloud coverage over land and ocean under global warming

Huan Liu¹, Ilan Koren¹, Orit Altaratz¹, Mickaël D. Chekroun¹

¹Department of Earth and Planetary Sciences, Weizmann Institute of Science, Rehovot, 76100, Israel

5 *Correspondence to:* Ilan Koren (ilan.koren@weizmann.ac.il)

Abstract. Clouds play a key role in Earth's energy budget and water cycle. Their response to global warming contributes the largest uncertainty to climate prediction. Here, by performing an empirical orthogonal function analysis on 42 years of reanalysis data of global cloud coverage, we extract [an unambiguous](#) trend and [El Niño-Southern Oscillation](#)-associated modes. The trend mode translates spatially to [decreasing trends](#) in cloud coverage over most continents and [increasing trends](#) over the tropical and subtropical oceans. A reduction in near-surface relative humidity can explain the decreasing trends in cloud coverage over land. Our results suggest potential stress on the terrestrial water cycle and changes in the energy partition between land and ocean, all associated with global warming.

1 Introduction

15 Clouds cover more than 60 % of the Earth's surface. They play a critical role in the global water cycle (Bengtsson, 2010) and act as the primary energy gatekeepers for the climate system by reflecting incoming solar radiation and blocking outgoing terrestrial radiation (Stephens et al., 2012). Overall, clouds cool the surface at a rate of approximately 20 W m⁻² (Stephens et al., 2012).

20 One of the most pressing needs in climate prediction is to clarify whether and how global warming impacts clouds on a global scale and to delineate the mechanisms at play (Zelinka et al., 2020). A common practice for addressing this question consists of analyzing cloud feedbacks that can either amplify (positive feedback) or dampen (negative feedback) surface warming. However, estimating the overall cloud feedback is a challenging task since the net radiative effect depends on the type, geographical location, vertical extent, lifetime, and optical properties of clouds (Chen et al., 2000). So far, estimations of clouds' responses to the warming trend is inconclusive (Aerenson et al., 2022; Forster et al., 2021). To partly address this issue, we explore the influence of climate change on global cloud coverage, which is, of course, one of the most crucial cloud factors.

25 Previous works that examined [tendencies](#) in cloud coverage under a warmer climate show substantial discrepancies among them (Gettelman and Sherwood, 2016; Ceppi et al., 2017; Zelinka et al., 2020). Even estimations for the same cloud type vary between studied periods, locations, datasets, and models ([e.g., Norris and Evan, 2015](#); Zhou et al., 2016; Zelinka et al., 2017; [Karlsson and Devasthale, 2018](#)). [Key](#) factors [in](#) these discrepancies are related to data uncertainties due to

删除[L]: e

删除[M]: clear

删除[L]: a

删除[L]: an

删除[L]: trends

删除[L]: ; Norris et al., 2016; Karlsson and Devasthale, 2018

删除[M]: Important

删除[M]: leading

删除[L]:

删除[M]: to

30 measurement errors in observational al datasets, on one hand (Chepfer et al., 2014), and the unsatisfactory representation of clouds in climate models, on the other (Stevens et al., 2013). For example, long-term surface observations, such as cloud coverage from the International Comprehensive Ocean–Atmosphere Data Set (ICOADS, Freeman et al., 2017) and the Extended Edited Cloud Reports Archive (EECRA, Hahn and Warren, 1999; Hahn et al., 2012), suffer from non-uniform sampling, changes in the synoptic-code format and stations, and limited coverage (e.g., Eastman et al., 2011; Aleksandrova et al., 2018). On the other hand, long-term satellite records, such as cloud coverage from the International Satellite Cloud Climatology Project (ISCCP, Rossow and Schiffer, 1999), the Pathfinder Atmospheres–Extended dataset (PATMOS-X, Heidinger et al., 2014), and the cloud component in the European Space Agency’s (ESA) Climate Change Initiative (CCI) programme (Cloud cci, Stengel et al., 2017), suffer from changing view geometries and orbit drifts (e.g., Evan et al., 2007; Norris and Evan, 2015). While attempts are being made to correct some of these issues in satellite observations, those

35 corrections may remove actual cloud tendencies at a global scale (e.g., Norris and Evan, 2015; Norris et al., 2016). In addition, those corrected products show significant discrepancies between linear trends in their cloud coverage (Norris and Evan, 2015). As for climate models, the representation of clouds in a coarse resolution grid is subordinate to the small-scale parameterization schemes employed, accounting in a limited way for the full range of scales involved therein (Zelinka et al., 2016; Zelinka et al., 2020).

40 Besides the uncertainties tied to observations and modeling, the sensitivity of clouds to temperature patterns (Zhou et al., 2016) and other large-scale climate drivers (Manaster et al., 2017; Gulev et al., 2021) can also lead to discrepancies between estimations of cloud coverage trends over different periods and regions. One example is found in the El Niño–Southern Oscillation (ENSO), a dominant mode of climate variability with seasonal-to-interannual time scales, traditionally emerging over the Tropical Pacific Ocean (Neelin et al., 1998). Through the strong coupling between the Pacific Ocean and the atmosphere above, ENSO's impact goes beyond the Pacific (Taschetto et al., 2020) and modulates global temperatures and cloud features (Davey et al., 2014; Yang et al., 2016). Thus, the ENSO signal often stands out as a major driver of variability in climate records, blurring the global-warming related trend, and even biasing its magnitude on decadal time scales (Compo and Sardeshmukh, 2010) due to the ENSO's low-frequency variability (Hope et al., 2017). Similarly, other large-scale climate phenomena, such as the Atlantic Multi-decadal Oscillation and the Pacific Decadal Oscillation, are natural climate

50 variability candidates that perturb global temperatures (Deser et al., 2010) and cloud coverage (Li et al., 2021). Therefore, they may introduce additional bias into global-warming related trends.

Despite the challenges, recent advancements in assimilation techniques and computing power have led to the production of high-quality reanalysis data. The latest version is the 5th generation of Atmospheric Reanalysis data from the European Centre for Medium-Range Weather Forecasts (ERA5), which offers uniformly sampled, long-term data of the atmosphere (Hersbach et al., 2019). To investigate the dominant processes that affect cloud coverage and examine the details both in the spatial and temporal domains, we analyze modes of variability in global cloud coverage by performing an Empirical Orthogonal Function (EOF) decomposition on 42 years (1979–2020) of ERA5 data (Hersbach et al., 2020); see Sect. 2. To evaluate the extent to which ERA5 captures climate variability and set the stage with fields having a well-studied reference,

60

- 删除[L]: s
- 删除[L]: the
- 删除[L]: station migrations
- 删除[L]: Warren et al., 2007;
- 删除[L]: ,
- 删除[L]: while
- 删除[L]:
- 删除[L]: ed
- 删除[L]: product
- 删除[L]: o
- 删除[L]: grid
- 删除[L]: ttempting to a
- 删除[L]: potential obstacles
- 删除[L]: and to
- 删除[L]: e

we analyze the global Surface air Temperature (ST, the air temperature at 2 meters above the surface) together with the Total Cloud Cover (TCC, the part of a grid box covered by clouds).

2 Materials and Methods

2.1 Dataset

The study uses three datasets: (1) 42 years (1979–2020) of monthly atmospheric data from ERA5 (<https://www.ecmwf.int/en/forecasts/datasets/reanalysis-datasets/era5>, Hersbach et al., 2020), which include ST, TCC, Land-Sea Mask (LSM) and Surface Pressure (SP) at single levels, as well as Relative Humidity (RH), Specific Humidity (SH), Temperature (T), vertical velocity (ω), U-wind component (U), V-wind component (V), wind Divergence (Div), Potential Vorticity (PV), and Relative Vorticity (RV) at 23 standard pressure levels (1000, 975, 950, 925, 900, 875, 850, 825, 800, 775, 750, 700, 650, 600, 550, 500, 450, 400, 350, 300, 250, 225 and 200 hPa). The original horizontal resolution of all ERA5 data is 0.25° ; (2) 18 years (2003–2020) of daily Cloud Fraction (CF) data observed by the MODerate resolution Imaging Spectroradiometer (MODIS) onboard the Aqua satellite (https://search.earthdata.nasa.gov/search?q=MYD08_D3, Platnick et al., 2003), with a horizontal resolution of 1° ; and (3) 44 years (1978–2021) monthly Niño-3.4 index from the National Oceanic and Atmospheric Administration center for Weather and Climate Prediction (https://origin.cpc.ncep.noaa.gov/products/analysis_monitoring/ensostuff/ONI_change.shtml).

ERA5 is a state-of-the-art reanalysis dataset and has been validated as the most reliable one for climate trend assessment (Gulev et al., 2021). In ERA5, the cloud fields are calculated using prognostic equations based on assimilated meteorological (thermodynamic and dynamic) variables that are optimally constrained by observations (Hersbach et al., 2019). The TCC is then calculated as a diagnostic parameter based on the prognostic cloud cover field using a generalized cloud overlap assumption based on a stochastic cloud generator. This assumption means that the degree of overlap between two cloudy layers becomes more random as the vertical distance between the layers increases; see more details in Barker (2008). The calculated TCC has been shown to essentially capture the spatiotemporal characteristics of measured cloud coverage on climatic (Yao et al., 2020) and weather scales (Binder et al., 2020).

2.2 Data Processing

Apart from the calculation of the Oceanic Niño Index (ONI, Glantz and Ramirez, 2020), the entire analysis is based on annual data and anomalies. The annual data is calculated as a simple average of monthly data for each calendar year. The annual anomaly is the deviation of the annual data from the mean over 1979–2020. ONI is calculated as the 3 month running mean of the monthly Niño-3.4 index.

Near-Surface Relative Humidity (RH_{NS}) is calculated here as RH_v at 950 hPa over the ocean and at 50 hPa above surface over land. Ocean is identified as grid boxes with a LSM-value no larger than 0.2, and land is identified as grid boxes with a LSM-

删除[L]: kin

删除[L]:). ST, in ERA5, is the theoretical temperature of

删除[L]: 1

删除[L]: his study

删除[L]: uses the

删除[L]: A

删除[L]: the European Centre for Medium-Range Weather

删除[L]: ERA5,

设置格式[L]: 字体颜色: 自动设置

删除[L]: , with a horizontal resolution of 0.25°

删除[L]: .

删除[L]: c

删除[L]: f

删除[L]: reanalysis dataset

删除[L]: CC is calculated as a prognostic cloud cover

删除[L]: corresponding

删除[L]: cover

删除[L]: in ERA5 is

删除[L]: estimat

删除[L]: by

删除[L]: calculated using thermodynamic conditions that

删除[L]: state-of-the-art

删除[L]: , providing uniformly sampled, long-term data o

删除[L]: Convective clouds are parameterized by a bulk r

删除[L]: In particular, t

删除[L]: was

删除[L]: be in good agreement with the

删除[L]: ages

value larger than 0.2. For each land grid box, its RH_{NS}-value is estimated based on a pressure-difference weighted linear interpolation given by the following equation:

$$\underline{RH_{NS-land}} = \frac{|P_1 - SP| \times RH_{P_2} + |P_2 - SP| \times RH_{P_1}}{|P_1 - P_2|}$$

where P₁ and P₂ are the adjacent standard pressure levels that contain the pressure level of 50 hPa, smaller than the local SP.

2.3 Area and TCC Weighting

Since the area of each 0.25 ° by 0.25 ° gridbox, as used in this study, depends on latitude, we performed an area weighting for all spatial averages. The area of each grid box is calculated as the product of arc lengths at the corresponding latitude and longitude by regarding the Earth as an oblate spheroid with a radius of 6378.137 km at the equator and 6356.752 km at the poles. In addition, we performed a TCC weighting to account for the spatial dependence of cloud coverage when assessing cloud-related processes. The TCC weights are given in Fig. 2c.

2.4 EOF Analysis

EOF analysis is a decomposition method of multivariate signals that is widely used in meteorology and oceanography (Lorenz, 1956; Preisendorfer and Mobley, 1988), to study possible spatial modes (i.e., patterns) of variability and how they change with time. It decomposes any given spatiotemporal field into a set of independent EOF modes in the spatial domain whose temporal variations are encoded by the corresponding Principal Components (PCs). With the proper interpretations, these independent modes can provide useful clues about the physics and dynamics of the investigated system (Schnur et al., 1993; Dunkerton, 1993; Dror et al., 2021). More specifically, EOFs and PCs come in pairs and are ordered by the corresponding variance that is explained by each given mode. The number of EOF-PC pairs is determined by the temporal dimension of the input data (42 for the annual ST and TCC anomalies considered here).

In this study, we used area-weighted data for the EOF analysis of annual ST and TCC anomalies to isolate the main drivers of global surface air temperature and cloud coverage. The area weighting is required in order to lessen the contribution of smaller-size grid boxes (Baldwin et al., 2009). Once the EOF analysis is performed on the area-weighted ST and TCC data, the final EOF modes presented in the main text are rescaled by dividing them by the corresponding area weights. The underlying EOF analysis is performed using the Python library, eofs (Version 1.4.0, <https://github.com/ajdawson/eofs>, Dawson, 2016).

3 Results

First to set the stage and to explore modes and sensitivities in the ERA5 TCC data as compared to direct measurements, we conducted an area-weighted EOF analysis on annual TCC anomalies and compared it with the observed CF from MODIS;

删除[L]: is considered continental,

删除[L]: and

删除[L]: calculated

删除[L]: using the RH-values at the adjacent pressure levels

删除[L]: by

删除[L]: . The pressure-values at those layers are calculat

设置格式[L]: 正文, 居中, 段落间距段前: 0.5 行, 段后: (

设置格式[L]: 默认段落字体, 字体: (默认) Times Nev

设置格式[L]: 默认段落字体, 字体: (默认) Times Nev

设置格式[L]: 默认段落字体, 字体: (默认) Times Nev

设置格式[L]: 默认段落字体, 字体: (默认) Times Nev

设置格式[L]: 默认段落字体, 字体: (默认) Times Nev

设置格式[L]: 默认段落字体, 字体: (默认) Times Nev

设置格式[L]: 默认段落字体, 字体: (默认) Times Nev

设置格式[L]: 默认段落字体, 字体: (默认) Times Nev

设置格式[L]: 字体颜色: 自动设置

设置格式[L]: 默认段落字体, 字体: (默认) Times Nev

设置格式[L]: 字体颜色: 自动设置

删除[L]:

设置格式[L]: 字体颜色: 自动设置

设置格式[L]: 默认段落字体, 字体: (默认) Times Nev

删除[L]: 1

删除[L]: 1

删除[L]: 1

删除[M]: n approach

删除[M]:

删除[M]: important

删除[M]: 1.5 ONI

see Fig. 1. To mimic the MODIS CF observations, we resampled ERA5 TCC data to a grid with a horizontal resolution of 1° and considered only a subset of data between 60°S to 60°N during 2003–2020. Figure 1 shows the three dominant EOF modes and PCs of the annual ERA5 TCC and MODIS CF anomalies. The very similar explained variance, spatial patterns in EOFs, and time evolution in PCs suggest that although ERA5 TCC is a simulated parameter, the model and assimilation techniques are able to reproduce essential variations of observed cloud coverage.

删除[O]: a grid with a

删除[L]:

Then, we extend the study period to 1979–2020 based on ERA5 data with a horizontal resolution of 0.25°. Figures 2a and 2c show the geographical distributions of annual mean ST and TCC data. It reveals the nearly uniform temperature gradient towards the poles and the expected patterns of high cloud coverage over the tropics and marine mid-latitudes and the extremely low cloud coverage over the deserts. Figures 2b and 2d plot the area-weighted global mean ST and TCC data; see

删除[L]: 1

删除[L]: 1

删除[L]: , averaged over the period 1979–2020

Sec. 2. The increasing ST trend represents clear signature of global warming (Eyring et al., 2021). In contrast, the lack of a consistent trend in TCC suggests that perturbations other than a warming climate might dominate the global TCC variability.

删除[L]: 1

删除[L]: 1

To identify and isolate the main underlying drivers in the variations, we perform again an area-weighted EOF analysis on annual ST and TCC anomalies. The results reveal spatio-temporal fields sufficient for identifying modes of variability driven by distinct physical processes. For each analyzed variable, these results exhibit spatial patterns captured by EOF modes,

删除[L]: of annual

删除[L]: observed

whose temporal variations are encoded by the corresponding PC (Lorenz, 1956). By analyzing the PC's time-variability, we are able to find correspondences between the EOF modes and known climate phenomena (Preisendorfer and Mobley, 1988).

删除[M]: evidence

删除[M]: evident

Notably, unlike EOF modes, physical processes are not necessarily orthogonal, and variations caused by one physical process could be split into different EOF modes, a phenomenon known as signal leakage (Richman, 1986). However, this issue is negligible for the dataset at hand, in particular for the dominant EOF modes of ST and TCC discussed below; see fig.

删除[L]: observed

删除[L]: ; see Sec. 2

S1 and Supplementary Text 1.

To set the stage, we first present our findings for the global surface air temperature. Figure 3 shows the two dominant EOF modes of the annual ST anomaly along with their PCs. Recall that a given PC encodes the temporal variability captured by the corresponding EOF mode, whose spatial features specify, in turn the magnitude and direction of the PC over each region.

删除[L]: 2

删除[L]: 2

For the dataset at hand, the leading EOF mode of ST (EOF1, Fig. 3a) accounts for 32.5% of the total variance and distills a consistent warming trend (PC1, Fig. 3b) over nearly all continents and most oceans (red shades in Fig. 3a). Its PC evolves almost synchronously with the annual global mean ST (black curve in Fig. 3b).

删除[L]: 28.3

删除[L]: 2

删除[L]: 2

This leading EOF mode reveals some regional features of the recent warming climate, such as the most significant warming being over the Arctics (Serreze and Barry, 2011), the nearly twice larger warming rate over land than over the ocean (Byrne and O’Gorman, 2018), and the feeble warming or even cooling signal over parts of the North Atlantic Ocean, the southeast Pacific Ocean, and the Southern Ocean (Keil et al., 2020; Heede and Fedorov, 2021; Bintanja et al., 2013). These features highlight that regional feedbacks can modify the warming pattern and lead to non-uniform warming.

删除[L]: 2

删除[L]: 2

删除[L]: 11.1

The second component of ST variations (EOF2, Fig. 3c), accounting here for 10.5% of the total variance, manifests itself as an ENSO-associated mode. This feature becomes strikingly apparent when comparing its PC (PC2, Fig. 3d) with the ONI, a common measure of ENSO (Glantz and Ramirez, 2020); see black curve in Fig. 2d and Supplementary Text 2. An episode

删除[L]: 2

删除[L]: Sec. 2.

155 of large positive values in PC2 coincides with large positive ONI-values, indicative of El Niño events. Analogously, episodes of large negative values for this PC2 coincide with large negative ONI-values, corresponding to La Niña events (Neelin et al., 1998).

As expected, EOF2 for ST shows strong positive anomalies over the central and Eastern tropical Pacific and negative anomalies over the Western Pacific. Furthermore, beyond the Pacific Ocean, ST over areas with strong negative (e.g., North America and the adjacent North Atlantic Ocean) and positive (e.g., South Africa, parts of Asia, Australia, and a part of the Southern Ocean) anomalies also closely correlate to ENSO events. These findings are consistent with previous studies (Deser et al., 2010; Davey et al., 2014) and highlight ENSO as an essential driver of the global climate system (Taschetto et al., 2020).

160 Again, these results reassures that ERA5 performs well in capturing climate variability during the study period, and that the EOF analysis is effective at isolating the warming-associated mode from influence of other climate perturbations. Overall, the EOF analysis for ST demonstrates that the global warming trend and ENSO are the dominant factors in surface air temperature variability over the last 42 years.

We turn next to our EOF results of global cloud coverage. Figure 4 presents the two dominant EOF modes and the corresponding PCs of the annual TCC anomaly. The first thing to note is that similarly to ST findings, a trend and an ENSO-associated mode are identified but in opposite order. The EOF1 for TCC (Fig. 4a) shows an ENSO-associated behaviour with its PC (Fig. 4b), evolving almost in perfect synchrony with the ONI. While EOF2 (Fig. 4c) demonstrates a clear trend with its PC (Fig. 4d), which strongly correlates with the annual global mean ST (black curve in Fig. 4d; Spearman's $\rho = 0.88$, p-value = 3.28×10^{-14} , two-tailed t-test; see Supplementary Text 3).

This EOF1 for TCC shows that the global cloud coverage is greatly influenced by ENSO and accounts for 21.8 % of the total variance, similar as the results shown over 2003–2020 period; see Fig. 1. It suggests that maritime Southeast Asia and the Western Pacific are anti-correlated with the PC and hence the ONI (blue shades in Fig. 4a). Consequently, the cloud coverage in regions of positive anomalies over the central to eastern Pacific (red shades in Fig. 4a) has a tendency to increase during El Niño years and to decrease during La Niña years. Beyond the Pacific Ocean, the analysis reveals strong negative correlations over the tropical Atlantic Ocean and positive correlations over western Asia, part of South America, the Southern United States, and the adjacent North Pacific Ocean. The patterns revealed here are consistent with satellite observations for the ENSO forced precipitation tendency (Davey et al., 2014). Moreover, they agree well with previous studies showing similar ENSO-associated modes in cloud radiative effects and cloud coverage by simulations and corrected satellite records (Yang et al., 2016; Li et al., 2021).

180 After decoupling the ENSO-associated mode from TCC, an unambiguous trend mode (Fig. 4c) appears. This trend mode in TCC accounts for 14.4 % of the total variance and yields a PC evolving similarly to the one associated with the ST warming mode; see Fig. 3b. However, unlike the latter, whose warming pattern is expressed throughout the globe, patterns of TCC growth are shown over a major part of the ocean (red shades in Fig. 4c), while patterns corresponding to shrinking TCC occur over most of the continents (blue shades in Fig. 4c). More specifically, the tropical and subtropical oceans exhibit the most significant increasing trends; while for the continents, South and North America, the Congo Basin, most of Asia,

删除[I]: These

删除[I]: suggest

删除[L]: .

删除[L]: 3

删除[L]: 3

删除[L]: 3

删除[L]: 3

删除[L]: 3

删除[L]: 3

删除[L]: 6

删除[L]: 1

删除[L]: 65

删除[L]: 3

删除[M]: ,

删除[L]: Sec. 2

删除[L]: .

删除[M]: ,

删除[L]: 3

删除[L]: 3

删除[M]: will i

删除[L]: d

删除[M]: e

删除[L]: i

删除[M]: n

删除[L]: ,and vice versa

设置格式[M]: 删除线

删除[L]: frica

删除[M]: clear

190 Europe, and the poles exhibit a decreasing trend, the desert areas and the Indian subcontinent tend to display an increasing trend.

The reported trends are consistent with previously-made estimations based on long-term observations and historical simulations, such as the general decreasing trend over land revealed by surface observations (Warren et al., 2007), and the general increasing trend over tropics and eastern subtropics revealed by satellite observations and historical simulations (Norris and Evan, 2015; Zhou et al., 2016; Norris et al., 2016). Additionally, analysis in observed liquid water path from the Multisensor Advanced Climatology of Liquid Water Path (MAC-LWP) dataset yields increasing trends over most oceans (Manaster et al., 2017). These increasing patterns suggest consistent results with our findings as well because the value of liquid water path for cloud-free atmosphere is considered as 0. However, there are some contradictions with satellite observations, which show decreasing trends over most of the Congo Basin and increasing trends over most of the northeast part of tropical Atlantic (Norris and Evan, 2015). Also, some model-based future-climate prediction studies suggested a decrease in marine stratocumulus cloud coverage in warmer climate conditions (Forster et al., 2021; Zelinka et al., 2016).

200 By relying on the EOF analysis, we are able to identify an unambiguous signature of the warming climate on global cloud coverage. We explore next the potential thermodynamic drivers that could explain the revealed TCC trend. In that respect, we assess the correlation between each ERA5 meteorological variable (207 in total) and TCC by calculating the corresponding Spearman's ρ for the annual data in Fig. 5. Meteorological variables that are checked here including RH, SH, T, U, V, ω , Div, PV, and RV at 23 standard pressure levels ranging from 1000 to 200 hPa, see Sect. 2.

205 Figure 5a presents the average correlations over land (LSM > 0.2) and ocean (LSM \leq 0.2); see Sect. 2. These results show that RH, in most pressure levels, exhibits the strongest correlation with continental TCC, while for maritime TCC, RH and SH yield comparably strong correlations. A previous analysis based on satellite observations and other atmospheric reanalysis datasets obtained similar conclusions (Koren et al., 2010). The geographical distribution of the meteorological variables that best correlate with TCC, shown in Fig. 5b, further highlights RH as the strongest component over almost all continents. Moreover, there is no single variable besides RH that correlates strongly with nearly all continental TCC; see Fig. S2 and Supplementary Text 4. As for the maritime TCC, it exhibits a diversity of best correlated variables dominated by RH, SH, and PV. Such correlation differences over land and ocean may link to the different atmospheric conditions over land and ocean, as well as to the different dynamics of continental clouds and maritime clouds.

210 The RH correlation score shows a global peak over land (0.65 ± 0.20) and a local peak over the ocean (0.43 ± 0.22) slightly above the surface (925 hPa, the magenta arrow in Fig. 5a). RH, which, for a given pressure level, is a function of the specific humidity and the temperature, is a key parameter in determining cloud properties. Based on a parcel's theory describing convective cloud formation, the low-level RH will determine the likelihood of cloud formation and its extent. Moreover, low-level RH represent a more localized process, while high-level RH-values are likely to be affected by processes such as

220 cloud evaporation and long-distance water vapor transport (Bengtsson, 2010).

- 删除[M]: clear
- 删除[L]: agree
- 删除[I]: some
- 删除[L]: using
- 删除[L]: historical
- 删除[L]: ;
- 删除[L]: there is some contradiction with
- 删除[L]: , which
- 删除[M]: R
- 删除[L]: observe
- 删除[L]:
- 删除[M]: capture a clear
- 删除[M]:
- 删除[L]: observed
- 删除[L]: Specific Humidity (
- 删除[L]:)
- 删除[L]: Temperature (
- 删除[L]:)
- 删除[L]: U-wind component (
- 删除[L]:)
- 删除[L]: V-wind component (
- 删除[L]:)
- 删除[L]: vertical velocity (
- 删除[L]:)
- 删除[L]: wind divergence (
- 删除[L]:)
- 删除[L]: Potential Vorticity (
- 删除[I]:)

Therefore, to further explore the links between TCC and RH, we introduce a hybrid RH variable denoted as RH_{NS} , taking into account the terrestrial topography. RH_{NS} is defined as RH at 950 hPa over the ocean, and the RH at a pressure level of 50 hPa less than the local surface pressure over land, see Sect. 2.

Figure 6a shows the temporal trend in RH_{NS} for the study duration (1979–2020) using ordinary least-square regression analysis (Wells and Krakivsky, 1971). It shows a consistent decreasing trend in RH_{NS} over land at a rate of 1–2 % of relative humidity per decade, as well as similar spatial patterns in these RH_{NS} trends to those exhibited in the TCC trend mode. The statistically significant RH_{NS} trends lead to similar conclusions, see fig. S3 and Supplementary Text 5. The larger decreasing rate of RH_{NS} over the continents is expected due to the limited reservoir of water vapor and the larger warming rate over land; see Fig. 3a, and is consistent with previous studies that suggest a decreasing trend in surface air RH over land but only weak changes over ocean under a warmer climate (e.g., Byrne and O’Gorman, 2018). Figure 6b shows a map of the correlation between RH_{NS} and TCC, revealing a distinct difference between the high correlation scores for most of the continents (apart from the Sahara) compared to the oceans. The distributions of the correlations (Fig. 6c) show the high and relatively narrow correlation spread over land. Moreover, the global mean correlation of TCC with RH_{NS} shows the highest score of 0.69 ± 0.18 over land.

4 Discussion

Surface air temperature is likely to be the most explored variable with respect to climate change (Gulev et al., 2021). It is a direct measure of global warming on the most relevant level for most biological systems, and it characterizes the temperature interface between the ocean and land, and the atmosphere. As such, it sets boundary conditions for tropospheric processes. Clouds are at the heart of the water cycle and serve as the radiation modulators of the atmosphere (Bengtsson, 2010; Stephens et al., 2012). Though the overall effects on the fresh water and radiative budgets depend on cloud type and properties (Chen et al., 2000; Houze, 2014), the first variable to explore is the horizontal cloud extent, namely what fraction of the sky that is cloudy per each region on the globe.

By performing EOF analysis on ERA5 data over 1979–2020, we showed that the two dominant modes of surface air temperature and total cloud coverage can be described as a trend and an ENSO tendency. The order of these modes is flipped; for the surface air temperature, the trend leads the ENSO, while for cloud coverage, the trend follows the ENSO.

We used the frequently-explored surface air temperature data to set the stage and demonstrate the rich information that can be drawn from the modes. The temperature analysis reveals a clear trend captured by the leading PC paired with an almost totally red EOF mode (i.e., dominated by positive anomalies) of known regional features (Serreze and Barry, 2011; Byrne and O’Gorman, 2018; Keil et al., 2020; Heede and Fedorov, 2021; Bintanja et al., 2013). The second mode reveals a rich pattern of ENSO weights and signs over the entire globe, highlighting the fact that ENSO is a key driver of the global climate system (Neelin et al., 1998; Taschetto et al., 2020). The cloud coverage analysis shows a clear ENSO mode followed

删除[L]: the near-surface RH (

删除[L]:)

删除[L]: 5

删除[M]: clear,

删除[L]:

删除[L]: ⁻¹

删除[L]: 2

删除[L]: .

删除[L]: 5

删除[L]: contrast

删除[L]: 5

删除[M]: yields a

by a trend mode in terms of variance decomposition. The trend mode shows growth in cloud coverage with time over the tropical and subtropical oceans, while shrinking in cloud coverage is revealed over most non-desert continents.

删除[L]: The complex sensitivity of cloud coverage to ENSO could partly explain why it is challenging to find climate trends in clouds.

Because of the limited availability of water vapor sources over land, terrestrial clouds are more likely to be humidity-limited.

删除[L]: observed

255 Relative humidity measures how far a given specific humidity is from saturation per given temperature and pressure and is, therefore, a fundamental measure of cloud formation. In particular, relative humidity near the surface dictates the initial conditions of a rising air parcel. In a warming climate, over the continents, near-surface relative humidity is expected to decline (Byrne and O’Gorman, 2018) and is likely to affect cloud formation similarly. Over the warming oceans, for which the water vapor reservoir is not limited, enhanced evaporation can supply additional water vapor and hence partly cancel changes in relative humidity due to temperature increasing. Therefore, trends of near-surface relative humidity and their links to cloud coverage over the oceans are less distinct.

Our results have several implications. The more optimistic one is that increased cloud coverage over the central belt of the oceans implies a possible negative cloud feedback to global warming. The total effect will subsequently depend on how the increased cloud coverage is distributed among cloud types and their properties. Nevertheless, as a first approximation, larger 265 subtropical marine stratocumulus decks are likely to cause stronger cooling (Wood, 2012; Zelinka et al., 2017). In contrast, the consistent reduction in cloud coverage over land suggests an additional warming and larger stress on the freshwater supply that is already in shortage in many regions around the globe (Oki and Kanae, 2006). Moreover, such a contrast in cloud trends between land and ocean (Fig. 4c) suggests changes in the radiative energy partitioning between the two media that could be responsible for igniting additional feedbacks and changes in the atmospheric circulation.

删除[L]: In particular, the decrease in cloud coverage over the Amazon and Congo Basins, which contain the largest rainforests and the most precious and vulnerable ecosystems on our planet, is especially disconcerting (Langenbrunner et al., 2019; Bush et al., 2011; Lenton, 2011).

270 Supplementary information

Supplementary Text 1–5

删除[L]: 3

Figures S1–3

删除[M]: might ignite

Code and data availability

删除[L]: 2

275 All analysis is conducted by the programming language, Python (Version 3.7.0, <https://www.python.org/>). All data, documentation, and programming library used in analysis are publicly available (see websites in Sect. 2.).

删除[L]: 2

Author contribution

I.K. and H.L. designed the study. H.L. conducted the data analysis. O.A., I.K., H.L., and M.D.C. wrote the manuscript. All co-authors provided critical feedback and helped shape the research, conceptualization, investigation, and manuscript.

Competing interests

280 The authors declare that they have no conflict of interest.

Acknowledgments

This work has been supported by the European Research Council (ERC) under the European Union's Horizon 2020 research and innovation program (grant agreement No. 810370). This study was also partly supported by a Ben May Center grant for theoretical and/or computational research and by the Israeli Council for Higher Education (CHE) via the Weizmann Data
285 Science Research Center.

References

- Aerenson, T., Marchand, R., Chepfer, H., and Medeiros, B.: When will MISR detect rising high clouds?, *Journal of Geophysical Research: Atmospheres*, 127, 2021–035865, doi.org/10.1029/2021JD035865, 2022.
- [Aleksandrova, M., Gulev, S.K., and Belyaev, K.: Probability distribution for the visually observed fractional cloud cover over the ocean. *Journal of Climate*, 31, 3207–3232, doi.org/10.1175/JCLI-D-17-0317.1, 2018](#)
- 290 Baldwin, M.P., Stephenson, D.B., and Jolliffe, I.T.: Spatial weighting and iterative projection methods for eofs, *Journal of Climate*, 22, 234–243, doi.org/10.1175/2008J, 2009.
- [Barker, H.W.: Representing cloud overlap with an effective decorrelation length: An assessment using CloudSat and CALIPSO data. *Journal of Geophysical Research: Atmospheres*, 113, doi.org/10.1029/2008JD010391, 2008.](#)
- 295 Bengtsson, L.: The global atmospheric water cycle, *Environmental Research Letters*, 5, 025202, doi.org/10.1088/1748-9326/5/2/025002, 2010.
- [Binder, H., Boettcher, M., Joos, H., Sprenger, M., and Wernli, H.: Vertical cloud structure of warm conveyor belts—a comparison and evaluation of ERA5 reanalysis, CloudSat and CALIPSO data. *Weather and Climate Dynamics*, 1, 577–595, doi.org/10.5194/wcd-1-577-2020, 2020.](#)
- 300 Bintanja, R., van Oldenborgh, G.J., Drijfhout, S., Wouters, B., and Katsman, C.: Important role for ocean warming and increased ice-shelf melt in antarctic sea-ice expansion, *Nature Geoscience*, 6, 376–379, doi.org/10.1038/ngeo1767, 2013.
- [Byrne, M.P. and O'Gorman, P.A.: Trends in continental temperature and humidity directly linked to ocean warming, *Proceedings of the National Academy of Sciences*, 115, 4863–4868, doi.org/10.1073/pnas.172231211, 2018.](#)
- Ceppi, P., Briant, F., Zelinka, M.D., and Hartmann, D.L.: Cloud feedback mechanisms and their representation in global
305 climate models, *Wiley Interdisciplinary Reviews: Climate Change*, 8, 465, doi.org/10.1002/wcc.465, 2017.
- Chen, T., Rossow, W.B., and Zhang, Y.: Radiative effects of cloud-type variations, *Journal of climate*, 13, 264–286, doi.org/10.1175/1520-0442(2000)013<0264:REOCTV>2.0.CO;2, 2000.

删除[L]: Bush, M., Flenley, J., and Gosling, W.: *Tropical Rainforest Responses to Climatic Change*, Springer, Chichester, 2011.

- Chepfer, H., Noel, V., Winker, D., and Chiriaco, M.: Where and when will we observe cloud changes due to climate warming?, *Geophysical Research Letters*, 41, 8387–8395, doi.org/10.1002/2014GL061792, 2014.
- 310 Compo, G.P. and Sardeshmukh, P.D.: Removing ENSO-related variations from the climate record. *Journal of Climate*, 23, 1957–1978, doi.org/10.1175/2009JCLI2735.1, 2010.
- Davey, M., Brookshaw, A., and Ineson, S.: The probability of the impact of ENSO on precipitation and near-surface temperature, *Climate Risk Management*, 1, 5–24, doi.org/10.1016/j.crm.2013.12.002, 2014.
- Dawson, A.: Eofs: a library for eof analysis of meteorological, oceanographic, and climate data. *Journal of Open Research*
315 *Software*, 4, doi.org/10.5334/jors.122, 2016.
- Deser, C., Alexander, M.A., Xie, S.-P., and Phillips, A.S.: Sea surface temperature variability: patterns and mechanisms. *Annu. Rev. Mar. Sci*, 2, 115–143, doi.org/10.1146/annurev-marine-120408-151453, 2010.
- Dror, T., Chekroun, M.D., Altaratz, O., and Koren, I.: Deciphering organization of goes-16 green cumulus through the empirical orthogonal function (eof) lens, *Atmospheric chemistry and physics*, 21, 12261–12272, doi.org/10.5194/acp-21-
320 12261-2021, 2021.
- Dunkerton, T.J.: Observation of 3–6-day meridional wind oscillations over the tropical pacific, 1973–1992: vertical structure and interannual variability, *Journal of Atmospheric Sciences*, 50, 3292–3307, doi.org/10.1175/1520-0469(1995)052<1585:OODMWO>2.0.CO;2, 1993.
- Eastman, R., Warren, S.G., and Hahn, C.J.: Variations in cloud cover and cloud types over the ocean from surface
325 observations, 1954–2008. *Journal of Climate*, 24, 5914–5934, doi.org/10.1175/2011JCLI3972.1, 2011.
- Evan, A.T., Heidinger, A.K., and Vimont, D.J.: Arguments against a physical long-term trend in global ISCCP cloud amounts, *Geophysical Research Letters*, 34, doi.org/10.1029/2006GL028083, 2007.
- Eyring, V., Gillett, N.P., Achuta Rao, K.M., Barimalala, R., Barreiro Parrillo, M., Bellouin, N., Cassou, C., Durack, P.J.,
Kosaka, Y., McGregor, S., Min, S., Morgenstern, O., and Sun, Y.: In: Masson-Delmotte, V., Zhai, P., Pirani, A., Connors,
330 S.L., Pean, C., Berger, S., Caud, N., Chen, Y., Goldfarb, L., Gomis, M.I., Huang, M., Leitzell, K., Lonnoy, E., Matthews, J.B.R., Maycock, T.K., Waterfield, T., Yelekci, O., Yu, R., and Zhou, B. (eds.) *Human influence on the climate system*, pp. 423–552. Cambridge University Press, Cambridge, United Kingdom and New York, NY, USA, doi.org/10.1017/9781009157896.005, 2021.
- Forster, P., Storelvmo, T., Armour, K., Collins, W., Dufresne, J.-L., Frame, D., Lunt, D.J., Mauritsen, T., Palmer, M.D.,
335 Watanabe, M., Wild, M., and Zhang, H.: In: Masson-Delmotte, V., Zhai, P., Pirani, A., Connors, S.L., Pean, C., Berger, S., Caud, N., Chen, Y., Goldfarb, L., Gomis, M.I., Huang, M., Leitzell, K., Lonnoy, E., Matthews, J.B.R., Maycock, T.K., Waterfield, T., Yelekci, O., Yu, R., Zhou, B. (eds.): *The Earth’s energy budget, climate feedbacks, and climate sensitivity*, pp. 923–1054. Cambridge University Press, Cambridge, United Kingdom and New York, NY, USA, doi.org/10.1017/9781009157896.009, 2021.

- 340 [Freeman, E., Woodruff, S.D., Worley, S.J., Lubker, S.J., Kent, E.C., Angel, W.E., Berry, D.I., Brohan, P., Eastman, R., Gates, L., and Gloeden, W.: ICOADS Release 3.0: a major update to the historical marine climate record. *International Journal of Climatology*, 37, 2211–2232, doi.org/10.1002/joc.4775, 2017.](#)
 Gettelman, A., and Sherwood, S.C.: Processes responsible for cloud feedback, *Current climate change reports*, 2, 179–189, doi.org/10.1007/s40641-016-0052-8, 2016.
- 345 Glantz, M.H. and Ramirez, I.J.: Reviewing the oceanic Nino index (ONI) to enhance societal readiness for El Nino’s impacts, *International Journal of Disaster Risk Science*, 11, 394–403, doi.org/10.1007/s13753-020-00275-w, 2020.
 Gulev, S.K., Thorne, P.W., Ahn, J., Dentener, F.J., Domingues, C.M., Gerland, S., Gong, D., Kaufman, D.S., Nnamchi, H.C., Quaas, J., Rivera, J.A., Sathyendranath, S., Smith, S.L., Trewin, B., von Schuckmann, K., and Vose, R.S.: In: Masson-Delmotte, V., Zhai, P., Pirani, A., Connors, S.L., Pean, C., Berger, S., Caud, N., Chen, Y., Goldfarb, L., Gomis, M.I., Huang, M., Leitzell, K., Lonnoy, E., Matthews, J.B.R., Maycock, T.K., Waterfield, T., Yelekci, O., Yu, R., and Zhou, B. (eds.) *Changing state of the climate system*, pp. 287–422. Cambridge University Press, Cambridge, United Kingdom and New York, NY, USA, doi.org/10.1017/9781009157896.004, 2021.
[Hahn, C.J., and Warren, S.G.: Extended edited synoptic cloud reports from ships and land stations over the globe, 1952–1996, United States, doi.org/10.2172/12532, 1999.](#)
- 355 [Hahn, C.J., Warren, S.G., and Eastman, R.: Cloud Climatology for Land Stations Worldwide, 1971-2009 \(NDP-026D\) \(No. NPD-026D\), United States, doi: 10.3334/CDIAC/cli.ndp026d, 2012.](#)
 Heede, U.K. and Fedorov, A.V.: Eastern equatorial pacific warming delayed by aerosols and thermostat response to co2 increase, *Nature Climate Change*, 11, 696–703, doi.org/10.1038/s41558-021-01101-x, 2021.
 Hersbach, H., Bell, B., Berrisford, P., Biavati, G., Horanyi, A., Munoz Sabater, J., Nicolas, J., Peubey, C., Radu, R., Rozum, I., et al.: Era5 monthly averaged data on single levels from 1979 to present, Copernicus Climate Change Service (C3S) Climate Data Store (CDS) 10, 252–266, doi.org/10.24381/cds.f17050d7, 2019.
 Hersbach, H., Bell, B., Berrisford, P., Hirahara, S., Horanyi, A., Munoz-Sabater, J., Nicolas, J., Peubey, C., Radu, R., Schepers, D., Simmons, A., Soci, C., Abdalla, S., Abellan, X., Balsamo, G., Bechtold, P., Biavati, G., Bidlot, J., Bonavita, M., Chiara, G.D., Dahlgren, P., Dee, D., Diamantakis, M., Dragani, R., Flemming, J., Forbes, R., Fuentes, M., Geer, A.,
 365 Haimberger, L., Healy, S., Hogan, R.J., Holm, E., Janiskov, M., Keeley, S., Laloyaus, P., Lopez, P., Lupu, C., Radnoti, G., Rosnay, P.D., Rozum, I., Vamborg, F., Villaume, S., and Thepaut, J.-N.: The ERA5 global reanalysis. *Quarterly Journal of the Royal Meteorological Society*, 146, 1999–2049, doi.org/10.1002/qj.3803, 2020.
[Heidinger, A.K., Foster, M.J., Walther, A., and Zhao, X.T.: The pathfinder atmospheres–extended AVHRR climate dataset. *Bulletin of the American Meteorological Society*, 95, 909–922, doi.org/10.1175/BAMS-D-12-00246.1, 2014.](#)
- 370 Hope, P., Henley, B.J., Gergis, J., Brown, J., and Ye, H.: Time-varying spectral characteristics of ENSO over the last millennium. *Climate Dynamics*, 49, 1705–1727, doi.org/10.1007/s00382-016-3393-z, 2017.
 Houze Jr, R.A.: *Cloud Dynamics*, Academic press, Oxford UK, 2014.

Karlsson, K.-G., and Devasthale, A.: Inter-comparison and evaluation of the four longest satellite-derived cloud climate data records: Clara-a2, esa cloud cci v3, isccp-hgm, and patmos-x, *Remote Sensing*, 10, 1567, doi.org/10.3390/rs10101567, 2018.

375 Keil, P., Mauritsen, T., Jungclaus, J., Hedemann, C., Olonscheck, D., and Ghosh, R.: Multiple drivers of the north Atlantic warming hole. *Nature Climate Change*, 10, 667–671, doi.org/10.1038/s41558-020-0819-8, 2020.

Koren, I., Feingold, G., and Remer, L.A.: The invigoration of deep convective clouds over the atlantic: aerosol effect, meteorology or retrieval artifact?. *Atmospheric Chemistry and Physics*, 10, 8855–8872, doi.org/10.5194/acp-10-8855-2010, 2010.

380 Li, Y., Ge, J., Dong, Z., Hu, X., Yang, X., Wang, M., and Han, Z.: Pairwise-rotated eofs of global cloud cover and their linkages to sea surface temperature. *International Journal of Climatology*, 41, 2342–2359, doi.org/10.1002/joc.6962, 2021.

Lorenz, E.N.: *Empirical Orthogonal Functions and Statistical Weather Prediction*, Massachusetts Institute of Technology, Department of Meteorology Cambridge, Cambridge Massachusetts, 1, 1956.

385 Manaster, A., O'Dell, C.W., and Elsaesser, G.: Evaluation of cloud liquid water path trends using a multidecadal record of passive microwave observations. *Journal of Climate*, 30, 5871-5884, doi.org/10.1175/JCLI-D-16-0399.1, 2017.

Neelin, J.D., Battisti, D.S., Hirst, A.C., Jin, F.-F., Wakata, Y., Yamagata, T., and Zebiak, S.E.: ENSO theory, *Journal of Geophysical Research: Oceans*, 103, 14261–14290, doi.org/10.1029/97JC03424, 1998.

390 Norris, J.R., and Evan, A.T.: Empirical removal of artifacts from the isccp and patmos-x satellite cloud records, *Journal of Atmospheric and Oceanic Technology*, 32, 691–702, doi.org/10.1175/JTECH-D-14-00058.1, 2015.

Norris, J.R., Allen, R.J., Evan, A.T., Zelinka, M.D., O'Dell, C.W., and Klein, S.A.: Evidence for climate change in the satellite cloud record. *Nature*, 536, 72–75, doi.org/10.1038/nature18273, 2016.

Oki, T. and Kanae, S.: Global hydrological cycles and world water resources, *science*, 313, 1068–1072, doi.org/10.1126/science.1128845, 2006.

395 Platnick, S., King, M.D., Ackerman, S.A., Menzel, W.P., Baum, B.A., Riédi, J.C., and Frey, R.A.: The MODIS cloud products: algorithms and examples from Terra, *IEEE Transactions on geoscience and Remote Sensing*, 41, 459-473, doi.org/10.1109/TGRS.2002.808301, 2003.

Preisendorfer, R.W., and Mobley, C.D.: Principal component analysis in meteorology and oceanography, *Developments in atmospheric science*, 17, 1988.

Richman, M.B.: Rotation of principal components, *Journal of climatology*, 6, 293–335, doi.org/10.1002/joc.3370060305, 1986.

400 Rossow, W.B., and Schiffer, R.A.: Advances in understanding clouds from ISCCP. *Bulletin of the American Meteorological Society*, 80, 2261–2287, doi:10.1175/1520-0477(1999)080<2261:AIUCFI.2.0.CO;2, 1999.

Schnur, R., Schmitz, G., Grieger, N., and Von Storch, H.: Normal modes of the atmosphere as estimated by principal oscillation patterns and derived from quasigeostrophic theory, *Journal of the atmospheric sciences*, 50, 2386–2400, 405 doi.org/10.1175/1520-0469(1993)050<2386:NMOTAA>2.0.CO;2, 1993.

删除[L]: Langenbrunner, B., Pritchard, M., Kooperman, G.J., and Randerson, J.T.: Why does amazon precipitation decrease when tropical forests respond to increasing co2?, *Earth's future*, 7, 450–468, doi.org/10.1029/2018EF001026, 2019.

Lenton, T.M.: Early warning of climate tipping points, *Nature climate change*, 1, 201–209, doi.org/10.1038/nclimate1143, 2011.

删除[L]:

Serreze, M.C. and Barry, R.G.: Processes and impacts of arctic amplification: a research synthesis, *Global and planetary change*, 77, 85–96, doi.org/10.1016/j.gloplacha.2011.03.004, 2011.

[Stengel, M., Stapelberg, S., Sus, O., Schlundt, C., Poulsen, C., Thomas, G., Christensen, M., Carbajal Henken, C., Preusker, R., Fischer, J., and Devasthale, A.: Cloud property datasets retrieved from AVHRR, MODIS, AATSR and MERIS in the framework of the Cloud_cci project, *Earth System Science Data*, 9, 881–904, doi.org/10.5194/essd-9-881-2017, 2017.](#)

410

Stephens, G.L., Li, J., Wild, M., Clayson, C.A., Loeb, N., Kato, S., L'ecuyer, T., Stackhouse, P.W., Lebsock, M., and Andrews, T.: An update on earth's energy balance in light of the latest global observations, *Nature Geoscience*, 5, 691–696, doi.org/10.1038/ngeo1580, 2012.

Stevens, B., and Bony, S.: What are climate models missing?, *Science*, 340, 1053–1054, doi.org/10.1126/science.1237554, 2013.

415

Taschetto, A.S., Ummenhofer, C.C., Stuecker, M.F., Dommenges, D., Ashok, K., Rodrigues, R.R., and Yeh, S.-W.: ENSO atmospheric teleconnections, El Nino southern oscillation in a changing climate, 309–335, doi.org/10.1002/9781119548164.ch14, 2020.

Warren, S.G., Eastman, R.M., and Hahn, C.J.: A survey of changes in cloud cover and cloud types over land from surface observations, 1971–96. *Journal of climate*, 20, 717–738, doi.org/10.1175/JCLI4031.1, 2007.

420

Wells, D.E. and Krakiwsky, E.J.: The Method of Least Squares, Department of Surveying Engineering, University of New Brunswick, Fredericton N.B., 18, 1971.

Wood, R.: Stratocumulus clouds, *Monthly Weather Review*, 140, 2373–2423, doi.org/10.1175/MWR-D-11-00121.1, 2012.

Yang, Y., Russell, L.M., Xu, L., Lou, S., Lamjiri, M.A., Somerville, R.C., Miller, A.J., Cayan, D.R., DeFlorio, M.J., Ghan, S.J., Liu, Y., Singh, B., Wang, H., Yoon, J.-H., and Rasch, P.J.: Impacts of ENSO events on cloud radiative effects in preindustrial conditions: changes in cloud fraction and their dependence on interactive aerosol emissions and concentrations. *Journal of Geophysical Research: Atmospheres*, 121, 6321–6335, doi.org/10.1002/2015JD024503, 2016.

425

Yao, B., Teng, S., Lai, R., Xu, X., Yin, Y., Shi, C., and Liu, C.: Can atmospheric reanalyses (CRA and ERA5) represent cloud spatiotemporal characteristics?. *Atmospheric research*, 244, 105091, doi.org/10.1016/j.atmosres.2020.105091, 2020.

430

Zelinka, M.D., Zhou, C., Klein, S.A.: Insights from a refined decomposition of cloud feedbacks, *Geophysical Research Letters*, 43, 9259–9269, doi.org/10.1002/2016GL069917, 2016.

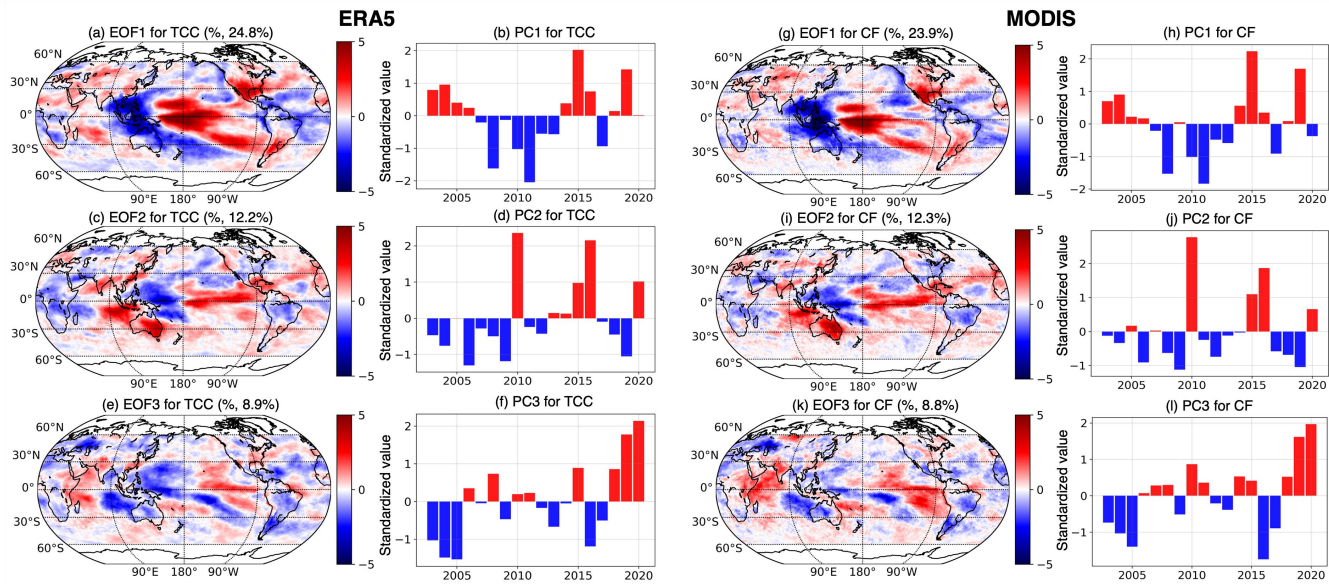
Zelinka, M.D., Randall, D.A., Webb, M.J., and Klein, S.A.: Clearing clouds of uncertainty, *Nature Climate Change*, 7, 674–678, doi.org/10.1038/nclimate3402, 2017.

435

Zelinka, M.D., Myers, T.A., McCoy, D.T., Po-Chedley, S., Caldwell, P.M., Ceppi, P., Klein, S.A., and Taylor, K.E.: Causes of higher climate sensitivity in cmip6 models, *Geophysical Research Letters*, 47, 2019–085782, doi.org/10.1029/2019GL085782, 2020.

Zhou, C., Zelinka, M.D., and Klein, S.A.: Impact of decadal cloud variations on the earth's energy budget, *Nature Geoscience*, 9, 871–874, doi.org/10.1038/ngeo2828, 2016.

删除[L]:



440 **Figure 1:** The three dominant EOF modes and their corresponding PCs of the annual cloud coverage anomaly (unit: %) from
 445 ERA5 (a–f) and MODIS (g–l) during 2003–2020. (a, g) The scaled leading EOF mode (EOF1, amplified by the standard
 deviation of its PC). (b, h) The standardized leading PC (PC1, divided by its standard deviation). (c, i) The scaled second
 EOF mode (EOF2). (d, j) The standardized second PC (PC2). (e, k) The scaled third EOF mode (EOF3). (f, l) The
 standardized third PC (PC3). The values given in the parenthesis of the title of panels a, c, e, g, i and k are the explained
 variances. The red and blue bars in panels b, d, f, h, j and l highlight the positive and negative PC values, respectively.

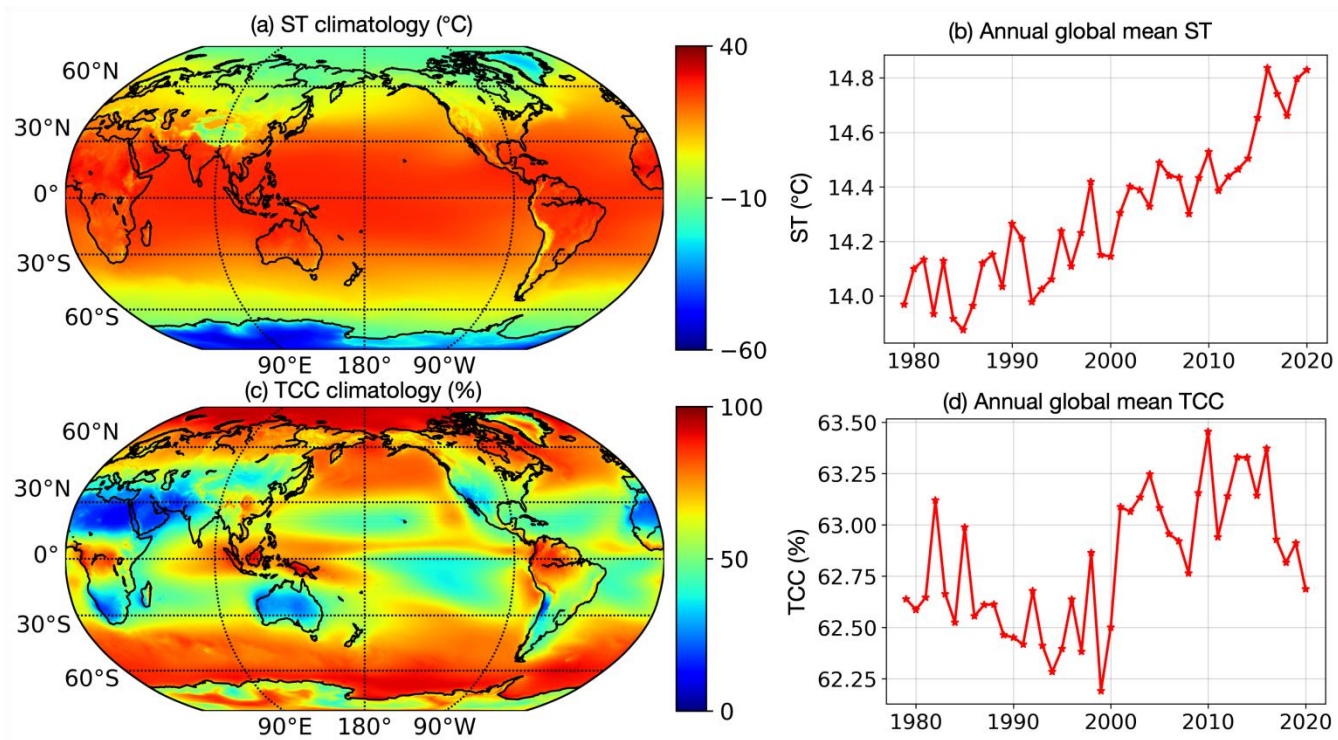
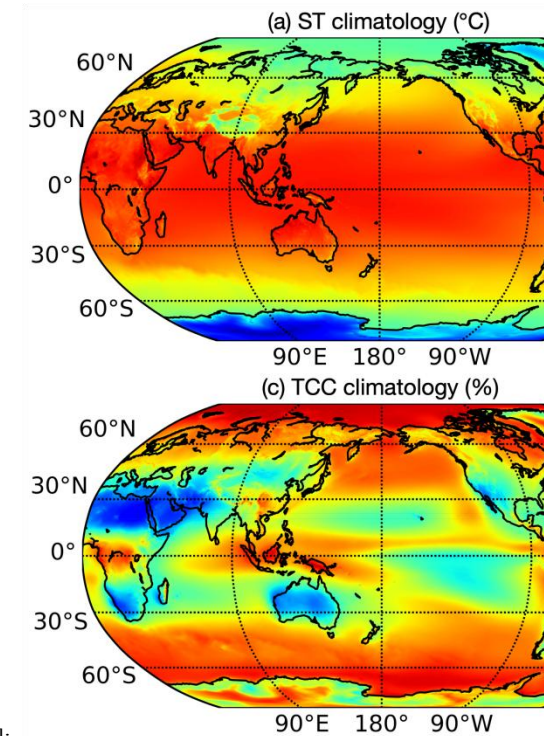


Figure 2: Climatological mean maps and the annual global means (area-weighted) of ST (unit: °C) and TCC (unit: %) during 1979–2020. (a) A global map of the climatological mean of ST. (b) Time series of the annual global mean of ST. (c) A global map of the climatological mean of TCC. (d) Time series of the annual global mean of TCC.



删除[L]:

删除[L]: 1

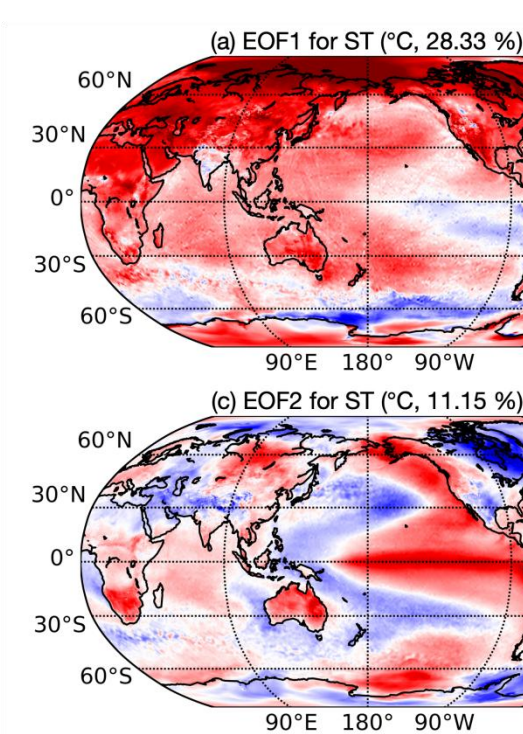
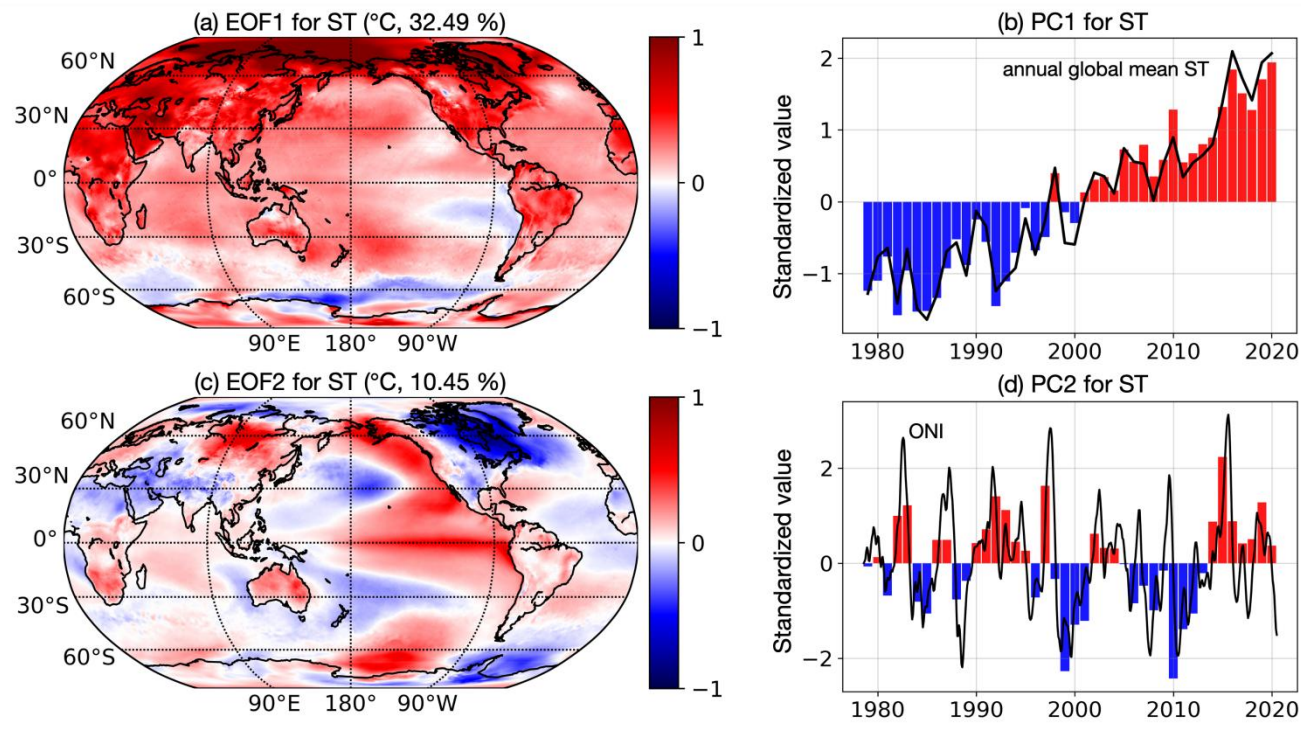


Figure 3: The two dominant EOF modes and their corresponding PCs of the annual ST anomaly (unit: °C) during 1979–2020. (a) The scaled leading EOF mode (EOF1, amplified by the standard deviation of its PC). (b) The standardized leading PC (PC1, divided by its standard deviation). (c) The scaled second EOF mode (EOF2). (d) The standardized second PC (PC2). The values given in the parenthesis of the title of panels a and c are the explained variances. The black curves in panels b and d are standardized annual global mean ST and ONI. The red and blue bars in panels b and d highlight the positive and negative PC-values, respectively.

删除[L]:

删除[L]: 2

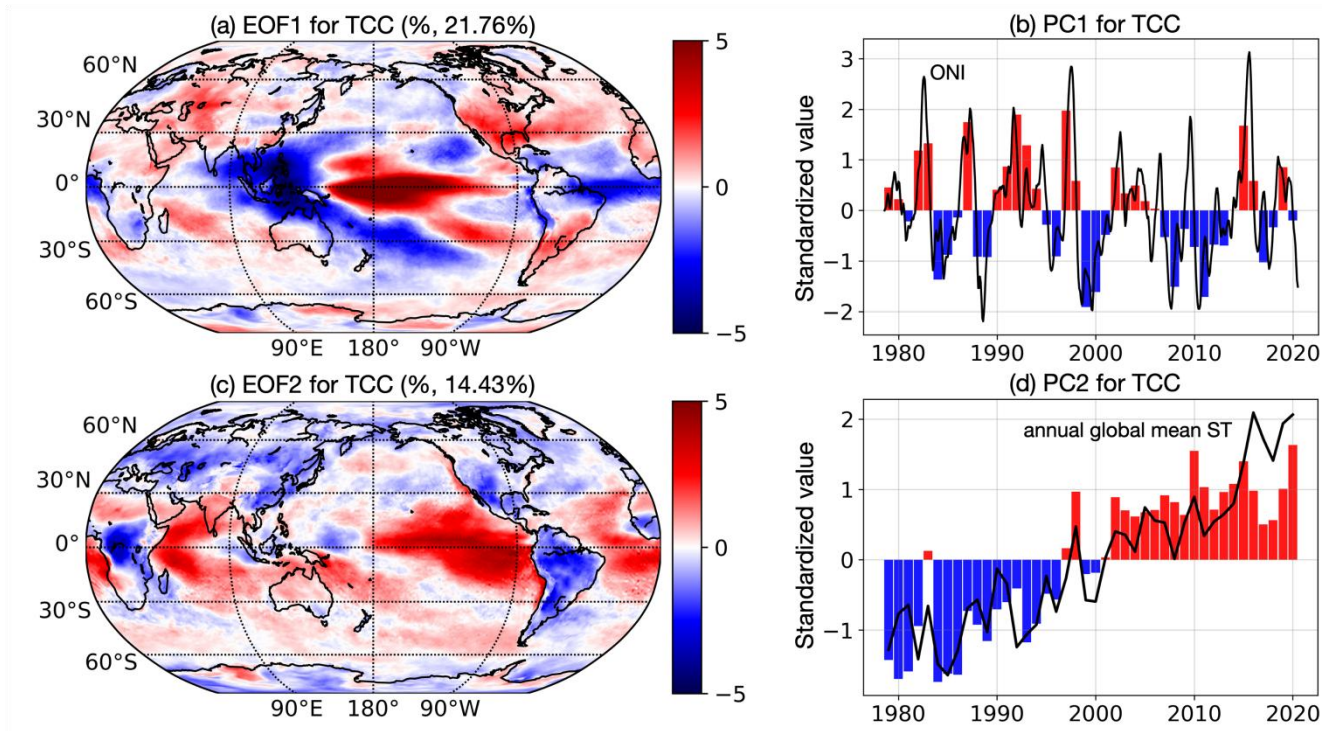


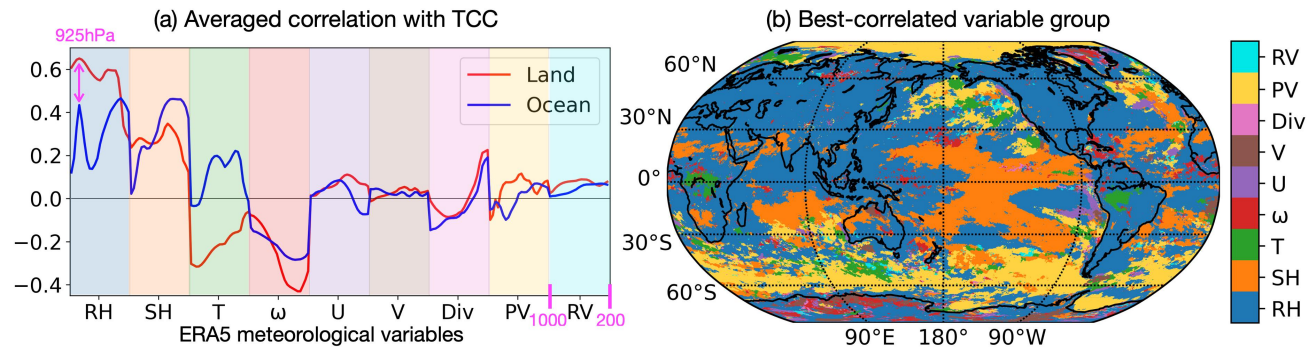
Figure 4: The two dominant EOF modes and their corresponding PCs of the annual TCC anomaly (unit: %) during 1979–2020. (a) The scaled leading EOF mode (EOF1, amplified by the standard deviation of its PC). (b) The standardized leading PC (PC1, divided by its standard deviation). (c) The scaled second EOF mode (EOF2). (d) The standardized second PC (PC2). The values given in the parenthesis of the title of panels a and c are the explained variances. The black curves in panels b and d are the standardized ONI and annual global mean ST, respectively. The red and blue bars in panels b and d highlight the positive and negative PC values, respectively.

删除[L]:

删除[L]: 3

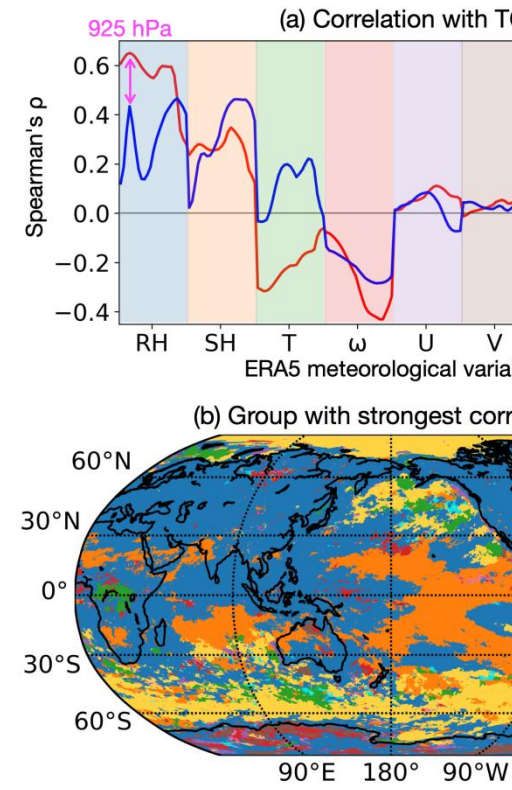
设置格式[L]: 左

465



470

Figure 5: The relationships between annual ERA5 meteorological variables and annual TCC during 1979–2020. (a) Averaged Spearman's ρ (area-TCC-weighted) over land and ocean; ρ -values are shown for RH, SH, T, U, V, ω , Div, PV, and RV at 23 standard pressure levels from 1000 to 200 hPa, starting from near the surface on the left part of the section (light color shades) to the upper atmosphere. (b) Map of the meteorological variables that best correlate with TCC, only Spearman's ρ that are statistically significant at the level of 0.05 (p -value < 0.05 , two-tailed t-test) are used.



删除[L]:
 删除[L]: 4
 删除[L]: 2
 删除[L]: 10

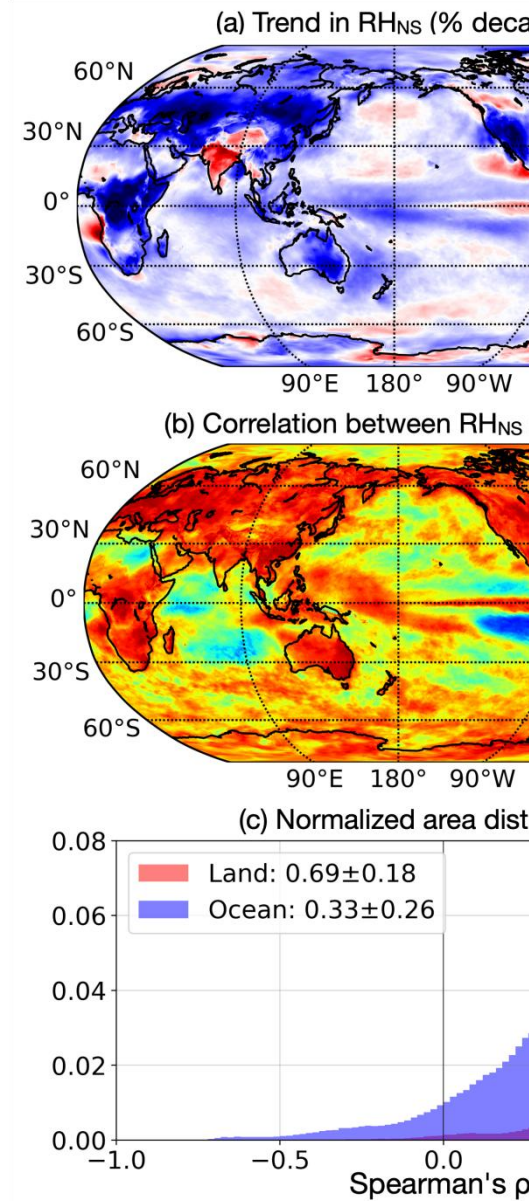
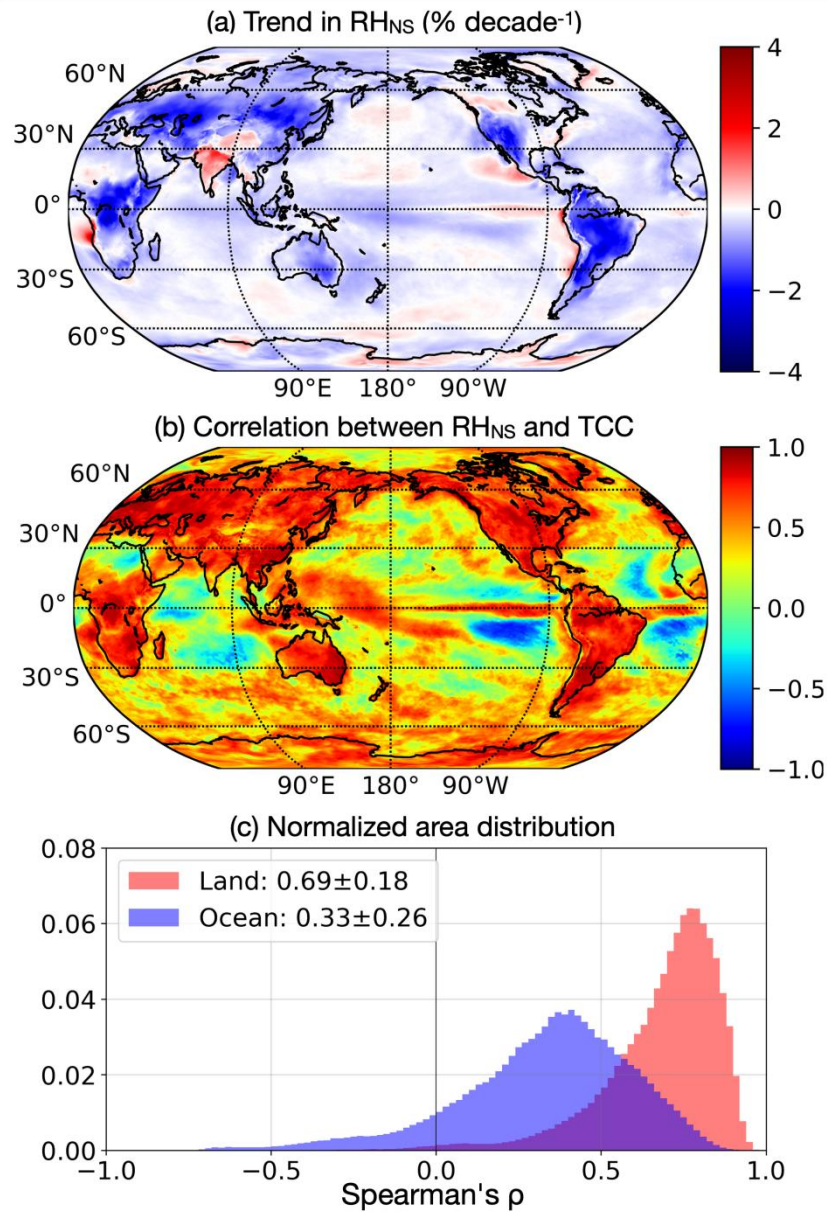


Figure 6: Trends in RH_{NS} and correlations between annual RH_{NS} and annual TCC. (a) A map of the temporal trend in annual RH_{NS} (unit: % decade⁻¹, where % denotes the absolute rather than the fractional percentage change). (b) A map of Spearman's ρ between RH_{NS} and TCC. (c) Distribution (area-TCC-weighted) of the correlations presented in panel b over land and ocean. The distribution's mean and standard deviation are displayed in the box.

475

删除[L]:

删除[L]: 5

设置格式[L]: 非上标/下标